



CERN-EP-2020-XXX  
October 2, 2020

## Production of $K_S^0$ , $\Lambda$ ( $\bar{\Lambda}$ ), $\Xi^\pm$ and $\Omega^\pm$ in jets and underlying events in pp and p-Pb collisions with ALICE

ALICE Collaboration\*

### Abstract

The production of strange hadrons ( $K_S^0$ ,  $\Lambda$ ,  $\Xi^\pm$  and  $\Omega^\pm$ ), baryon-to-meson ratios ( $\Lambda/K_S^0$ ,  $\Xi/K_S^0$  and  $\Omega/K_S^0$ ) and baryon-to-baryon ratios ( $\Xi/\Lambda$ ,  $\Omega/\Lambda$  and  $\Omega/\Xi$ ) are measured among inclusive, energetic jets and underlying events in pp collisions at  $\sqrt{s} = 13$  TeV and p-Pb collisions at  $\sqrt{s_{NN}} = 5.02$  TeV with the ALICE detector at the LHC. For the first time, we present results on multi-strange particles ( $\Xi^\pm$  and  $\Omega^\pm$ ) and corresponding ratios in jets and underlying events, providing an opportunity to test the strange particle production mechanism with a hard scattering. The  $p_T$  differential distribution of hadrons produced by jet is decrease slower than what is reported for inclusive one. The baryon-to-meson and baryon-to-baryon ratios in jets are clear different with the inclusive one in both collision systems at the intermediate  $p_T$  range. On the contrary, these ratios in underlying events show the same behavior with the inclusive one. When comparing hadron spectra and ratios within different centrality bins, the jet one are found to independent on the centrality. The results of this paper provide significant evidence that the jet fragmentation is not sufficient to describe strange and multi-strange particles production in hadronic collisions at LHC energies.

## 1 Introduction

High-energy heavy-ion (A-A) collisions are expected to create a deconfined system with extreme temperature and density, the Quark-Gluon Plasma (QGP) [1–7], in which the degrees of freedom are partonic, rather than hadronic. The structure and dynamical behavior of the QGP arise at the microscopic level from the interactions between quarks and gluons described by Quantum Chromodynamics (QCD) [8–10]. The interpretation of the heavy-ion results depends crucially on understanding results from small collisions systems such as proton-proton(pp) or proton-nucleus(p-A). In p-Pb collisions, there are not expected hot matter effects. So it is essential to investigate cold nuclear initial and final state effect to be used as the baseline for heavy-ion collisions [11, 12]. In pp collisions, there are not any hot and cold nuclear initial- and final-state effects. So it constitutes a baseline for the nuclear effects in both A-A and p-A collisions.

Several collective phenomena have been observed in high-multiplicity pp and p-Pb collisions that are reminiscent of the observation attributed to the creation of a medium in thermal and kinematic equilibrium in Pb-Pb collisions [13–19]. These include the long-range angular correlations on the near and away side studies, non-vanishing  $v_2$  coefficients in multi-particle cumulant studies, etc. In particular, in pp and p-Pb collisions, the baryon-to-meson ratios  $p/\pi$  and  $\Lambda/K_S^0$  have an enhancement at intermediate  $p_T$  ( $\sim 3$  GeV/c) [20–23] and the strange to non-strange hadron ratios have a significant enhancement with multiplicity [21, 23, 24], which is qualitatively similar to that observed in Pb-Pb collisions. The jet also constitute an important probe for the study of the QGP in heavy-ion collisions. On the contrary, several measurements show the absence of a robust nuclear effect on the jet production at mid-rapidity in small systems [25–32]. To better understand particle production mechanisms in small systems, the charged-particle jets are used to probe particle generated by hard scattering and those of the underlying events. It can help us to disentangle the soft and hard scattering contributions of baryon-to-meson or strange to non-strange enhancement in small systems.

The baryon-to-meson ratios are sensitive to quark and gluon jet production in heavy-ion collisions.

In this paper, the production of  $K_S^0$ ,  $\Lambda$  ( $\bar{\Lambda}$ ),  $\Xi^\pm$  and  $\Omega^\pm$  in jets and underlying events in pp at  $\sqrt{s} = 13$  TeV and p-Pb at  $\sqrt{s_{NN}} = 5.02$  TeV is reported. (Multi-)Strange particles are reconstructed in pseudo-rapidity range  $|\eta| < 0.75$ . Jets were reconstructed in the transverse momentum range  $p_{T,jet}^{ch} > 10$  GeV/c and in pseudo-rapidity range  $|\eta| < 0.75 - R$ , where  $R = 0.4$ . The (multi-)strange particles associated with jet are defined as a function of distance between particle and jets in  $\eta - \phi$  plane. The results presented in this paper significantly improve the precision, also show the centrality classes dependent and extend to multi-strange particle sector, with respect to our previous measurements in both pp (at different energy) and p-Pb collisions [? ]. The baryon-to-meson and baryon-to-baryon ratios in energetic jets are compared with the case of particles not associated with jets and PYTHIA 8 [33] simulation.

The paper is structured as follows. In Sec. 2, the ALICE apparatus and the data samples used for the analysis are presented. In Sec. 3, the procedure adopted for charged jet reconstruction, (multi-)strange particle reconstruction, and particle-jet matching strategy is described. The systematic uncertainties associated with the measurement are also studied in Sec. 3. The (multi-)strange hadron with  $p_T$  differential distributions, particle ratios with  $p_T$  distributions, the model comparisons, and an interpretation of the results are presented and discussed in Sec. 4. Finally, the paper is briefly summarised in Sec. 5.

## 2 ALICE Detector and data selection

A detailed description of the ALICE apparatus and its performance can be found in [34, 35]. This analysis relied on the central tracking systems and the forward VZERO system [36]. The forward two scintillator arrays V0A (covering pseudo-rapidity range of  $2.8 < \eta < 5.1$ ), and V0C ( $-3.7 < \eta < -1.7$ ) employed for both triggering detectors and determining the event multiplicity class. The main central

barrel detectors used for this analysis are the Inner Tracking System (ITS) [37], the Time Projection Chamber (TPC) [38] and the Time Of Flight detector (TOF) [39–42], which cover the pseudo-rapidity region  $|\eta| < 0.9$  and locate inside a large solenoidal magnet providing a 0.5 T magnetic field.

The innermost barrel detector is the ITS consisting of six cylindrical layers of high-resolution silicon tracking detectors using three different technologies. The two innermost layers are silicon pixel technology (SPD), covering  $|\eta| < 2.0$  and  $|\eta| < 1.4$ , respectively. The SPD was used to reconstruct the collision's primary vertex and short track segments, which called "tracklets". The four outer layers are based on silicon drift (SDD) and strip (SSD) detectors, with the outermost layer having a radius  $r = 43$  cm. The SDD and SSD are able to measure the specific energy loss ( $dE/dx$ ) with a relative resolution around 10%. The ITS is also used to reconstruct and identify low momentum particles down to 100 MeV/c that can not reach the TPC.

The TPC is a sizeable cylindrical drift detector which filled with a Ne – CO<sub>2</sub> gas mixture. The radius and the longitude of TPC is about  $85 < r < 250$  cm and  $-250 < z < 250$  cm, respectively. As the main tracking device, the TPC provides full azimuthal acceptance for tracks in the pseudo-rapidity region  $|\eta| < 0.9$ . In addition, it provides charged-hadron identification information via measurement of the specific ionization energy loss  $dE/dx$ . At low transverse momenta ( $p_T \lesssim 1.0$  GeV/c), the  $dE/dx$  resolution of 5.2% for a minimum ionizing particle allows a track-by-track identification. In contrast, at high transverse momenta ( $p_T \gtrsim 2.0$  GeV/c), the overlapping energy loss can still be statistically distinguished using a multi-Gaussian fit to the  $dE/dx$  distributions.

Outside of the TPC and located at a radius of approximately 4 m, the TOF measures the particles' time-of-flight. The TOF is a cylindrical array of multi-gap resistive plate chambers with an intrinsic time resolution of 50 ps. It covers the pseudo-rapidity range  $|\eta| < 0.9$  with (almost) full azimuthal acceptance. It can provide particle identification over a broad range at intermediate transverse momenta ( $0.5 \lesssim p_T \lesssim 2.7$  GeV/c). The total time-of-flight resolution, including the collision time resolution, is about 90 ps in pp collisions and approximately? in p–Pb collisions (some paper write as 100 ps. And how many for p–Pb?).

Data of pp collisions at  $\sqrt{s} = 13$  TeV and of p–Pb collisions at  $\sqrt{s_{NN}} = 5.02$  TeV is used in this analysis. The pp samples were recorded in 2016–2017 with ALICE. The p–Pb sample is collected in 2016. The data were collected with a minimum bias (MB) trigger requiring a hit in both V0 scintillators in coincidence with proton bunches' arrival from both directions. Interaction vertices are reconstructed by the extrapolation of ITS track segments towards the nominal interaction point. Pile-up events, due to multiple interactions in the triggered bunch crossing, are removed by exploiting the correlation between the number of pixel hits and the number of SPD tracklets. In addition, the coordinate of the primary vertex along the beam direction is within  $\pm 10$  cm with respect to the nominal interaction point (center of the ALICE detector). After event selection, the pp samples consist of 1.5 billion events. The interaction probability per single bunch crossing ranges between 2% and 14%. The integrated luminosity of  $\mathcal{L}_{int} = 9.38 \pm 0.47$  nb<sup>-1</sup> based on the visible cross section observed by the V0 trigger extracted from a van der Meer scan [43]. About 500 million events of p–Pb samples are selected, which correspond to an integrated luminosity of  $\mathcal{L}_{int} = 287$   $\mu$ b<sup>-1</sup>, with a relative uncertainty of 3.7% [44]. The p–Pb events were divided into three multiplicity classes based on the total charged deposited in the V0A (the Pb-going direction). The multiplicity intervals and their corresponding mean charged-particle density ( $dN_{ch}/d\eta$ ) measured at midrapidity ( $|\eta| < 0.5$ ) are given in Ref. [45].

### 3 Analysis

#### 3.1 Charged jet reconstruction

In this analysis, the FastJet package [46] is used to find jets using charged particles with the so-called anti- $k_T$  algorithm. The anti- $k_T$  algorithm is a commonly known jet finding algorithm that starts the clustering with the highest momentum particles, in contrast to the  $k_T$  algorithm, which does the opposite. The introduction of the algorithm can be found in [47]. Charged particles, which are used as the jet reconstruction inputs, are reconstructed using ITS and TPC information. The charged particles are selected in  $|\eta_{\text{trk}}| < 0.9$  (TPC acceptance) and  $p_T > 0.15$  GeV/c. The jet resolution parameter is  $R = 0.4$  and the reconstructed jet clusters are selected in  $|\eta_{\text{jet}}| < 0.35$ . A cut on charged-particle jet  $p_T$  ( $p_{T,\text{jet}}^{\text{ch}}$ ) is applied as  $p_{T,\text{jet}}^{\text{ch}} > 10$  GeV/c.

Besides the hard parton-parton interactions in the collisions, there is also the soft contribution summarizing everything that did not correlate with the hard collisions. The background density is around 1 GeV/c rad $^{-1}$  and is not subtracted on jet-by-jet basis in pp collisions. In p-Pb collisions, the reconstructed jet is further corrected for contributions from the underlying event to the jet momentum as

$$p_{T,\text{jet}} = p_{T,\text{jet}}^{\text{ch}} - \rho_{\text{bkg}} \cdot A_{\text{jet}} \quad (1)$$

where the  $p_{T,\text{jet}}^{\text{rec}}$  is the reconstructed jet  $p_T$ ,  $A_{\text{jet}}$  is the jet area and  $\rho_{\text{bkg}}$  is the event-by-event background density [48]. The  $A_{\text{jet}}$  is calculated using the Fastjet algorithm with the ghost area 0.005 [49]. A method that is suitable for combinatory jet background density ( $\rho_{\text{bkg}}$ ) estimation for sparse systems circumvents circumventing the problems arising from using the ghost jets is introduced in [50]. The basic idea is to neglect the ghosts and instead account for the empty areas by introducing a factor correcting the background density for it. It can be implemented by the following approach

$$\rho_{\text{bkg}} = C \cdot \text{median}\left\{\frac{p_{T,i}}{A_i}\right\}, \text{ with } C = \frac{\sum_j A_j}{A_{\text{acc}}} \quad (2)$$

Technically, the occupancy correction factor  $C$  is calculated as the ratio of  $k_T$  jet clusters built by pure ghosts overall  $k_T$  jet clusters. This method has the advantage that it uses the median and takes empty areas into account and that it does not have conceptual problems like other methods. This method can be further refined for the specific use case of p-Pb collisions. It can be shown that the exclusion of the first two  $k_T$  jets from Eq. (2) is enhancing the background quality.

#### 3.2 Strange particles reconstruction

The strange particles  $K_S^0$ ,  $\Lambda$ ,  $\bar{\Lambda}$ ,  $\Xi^\pm$  and  $\Omega^\pm$  are reconstructed at mid-rapidity ( $|\eta| < 0.75$ ) with their specific weak decay topology. The following decay channels are studied [51].

$$\begin{aligned} K_S^0 &\rightarrow \pi^+ + \pi^- & B.R. &= (69.20 \pm 0.05)\% \\ \Lambda(\bar{\Lambda}) &\rightarrow p(\bar{p}) + \pi^-(\pi^+) & B.R. &= (63.9 \pm 0.5)\% \\ \Xi^-(\bar{\Xi}^+) &\rightarrow \Lambda(\bar{\Lambda}) + \pi^-(\pi^+) & B.R. &= (99.887 \pm 0.035)\% \\ \Omega^-(\bar{\Omega}^+) &\rightarrow \Lambda(\bar{\Lambda}) + K^-(K^+) & B.R. &= (67.8 \pm 0.7)\% \end{aligned}$$

The proton, pion, and Kaon tracks (daughter tracks) are identified in the TPC via their measured energy deposition [35]. The identification methods for the  $V^0(K_S^0$  and  $\Lambda(\bar{\Lambda})$  which decay into two oppositely charged daughter particles) and cascade ( $\Xi^\pm$  and  $\Omega^\pm$  which decay into a charged meson (bachelor) plus a  $V^0$  decaying particle, giving the two-step process) candidates follow those presented in earlier ALICE publications [20, 24, 52–55]. In addition, to remove the contribution from pileup collisions outside the trigger proton bunch (out-of-bunch pileup), it is requested that at least one of the tracks from the decay

**Table 1:**  $V^0$ s ( $K_S^0$ ,  $\Lambda$  and  $\bar{\Lambda}$ ) candidate selection criteria of topological variable, daughter track and candidate. The DCA stands for “Distance of Closest Approach”, PV represents the “Primary collision Vertex” and CPA is the “Cosine Pointing Angle between the momentum vector of the reconstructed  $V^0$  and the displacement vector between the decay and primary vertices”.

Topological variable	pp	p-Pb
$V^0$ transverse decay radius	$> 0.5$ cm	$> 0.5$ cm
DCA of positive / negative track to PV	$> 0.06$ cm	$> 0.06$ cm
DCA between $V^0$ daughter tracks	$< 1.0\sigma$	$< 1\sigma$
CPA of $V^0$	$> 0.97$ ( $K_S^0$ ); $> 0.995$ ( $\Lambda$ )	$> 0.97$ ( $K_S^0$ ); $> 0.995$ ( $\Lambda$ )
<b>Track selection</b>		
Daughter track pseudo-rapidity interval	$ \eta  < 0.8$	$ \eta  < 0.8$
Daughter track $N_{\text{crossed rows}}$	$\geq 70$	$\geq 70$
Daughter Track $N_{\text{crossed rows}}/N_{\text{findable}}$	$\geq 0.8$	$\geq 0.8$
TPC $dE/dx$	$< 5\sigma$	$< 5\sigma$
<b>Candidate selection</b>		
Pseudo-rapidity interval	$ \eta  < 0.75$	$ \eta  < 0.75$
Proper lifetime ( $mL/p$ )	$< 20$ cm ( $K_S^0$ ), $< 30$ cm ( $\Lambda$ )	$< 20$ cm ( $K_S^0$ ), $< 30$ cm ( $\Lambda$ )
Competing mass for $K_S^0$	$> 0.005$ GeV/ $c^2$	$> 0.005$ GeV/ $c^2$
Competing mass for $\Lambda$	$> 0.010$ GeV/ $c^2$	$> 0.010$ GeV/ $c^2$

**Table 2:**  $\Xi^\pm$  and  $\Omega^\pm$  candidate selection criteria of topological variable, daughter track and candidate.

Topological variable	pp	p-Pb
Cascade transverse decay radius	$> 0.8(0.6)$ cm	$> 0.6$ cm
$V^0$ transverse decay radius	$> 1.4$ cm	$> 1.2$ cm
DCA (bachelor to PV)	$> 0.05$ cm	$> 0.04$ cm
DCA ( $V^0$ to PV)	$> 0.07$ cm	$> 0.06$ cm
DCA (positive / negative track to PV)	$> 0.04(0.03)$ cm	$> 0.03$ cm
DCA between $V^0$ daughter tracks	$< 1.6\sigma$	$< 1.5\sigma$
DCA (bachelor to $V^0$ )	$< 1.6(1.0)$ cm	$< 1.3$ cm
CPA of Cascade	$> 0.97$	$> 0.97$
CPA of $V^0$	$> 0.97$	$> 0.97$
$V^0$ invariant mass window	$\pm 0.006$ GeV/ $c^2$	$\pm 0.008$ GeV/ $c^2$
<b>Track selection</b>		
Daughter track pseudo-rapidity interval	$ \eta  < 0.8$	$ \eta  < 0.8$
Daughter track $N_{\text{crossed rows}}$	$\geq 70$	$\geq 70$
Daughter Track $N_{\text{crossed rows}}/N_{\text{findable}}$	$\geq 0.8$	$\geq 0.8$
TPC $dE/dx$	$< 5\sigma$	$< 4\sigma$
<b>Candidate selection</b>		
Pseudo-rapidity interval	$ \eta  < 0.75$	$ \eta  < 0.75$
Proper lifetime ( $mL/p$ )		$< 3 \times c\tau$
Competing mass	$8$ MeV/ $c^2$	$8$ MeV/ $c^2$

products of the (multi-)strange hadron understudy is matched in either the ITS or TOF detector. The selections used in this paper are summarized in Tab. 1, 2

The signal extraction is performed as a function of  $p_T$ . In each  $p_T$  interval, an invariant mass histogram is produced and filled with the corresponding counts. Then a Gaussian function is used to fit the peak, and a liner function is used to fit the combinatory background. This allows for the extraction of the mean ( $\mu$ ) and width ( $\sigma$ ) of the peak. A “peak” region is defined within  $\pm 6\sigma$  for  $V^0$ s and  $\pm 3\sigma$  ( $\pm 4\sigma$ ) for cascades in pp (and p-Pb) with respect to  $\mu$  for each  $p_T$  bin. The “background” regions are defined on both sides of that central region. The  $p_T$ -differential yields of (multi-)strange particles are extracted by fitting the background with a linear function extrapolated under the signal region. Examples of the invariant mass peaks for all particles are shown in Fig. 1.

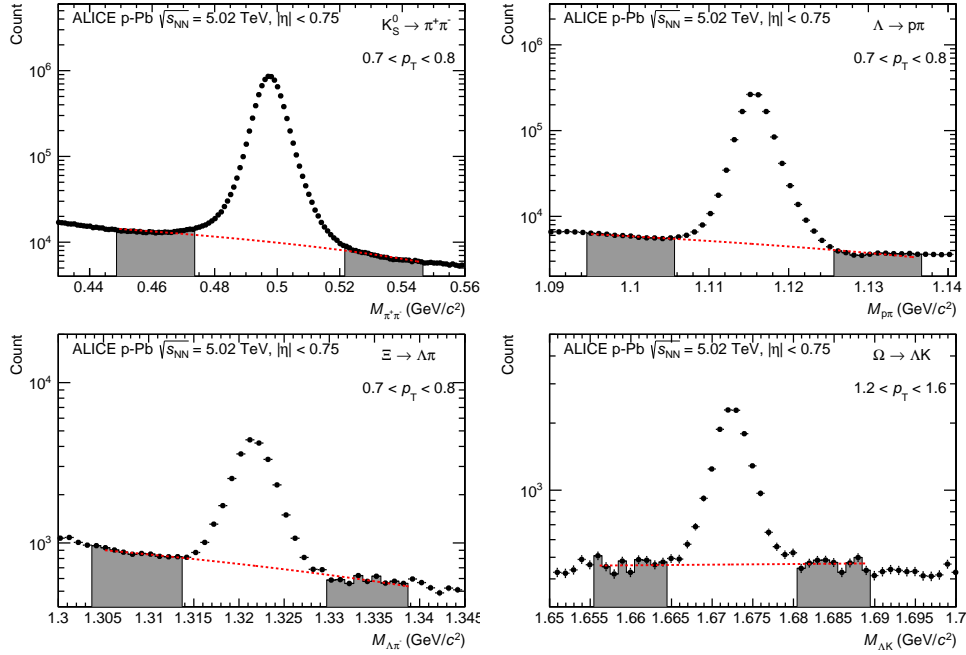


**Figure 1:** Invariant Mass distribution for  $K_S^0$ ,  $\Lambda$ ,  $\Xi$  and  $\Omega$  in different  $p_T$  intervals in MB p-Pb system. The candidates are reconstructed in  $|\eta| < 0.75$ . The grey areas are used for signal extraction in the bin counting procedure. The red dashed lines represent the fit to the background distributions and the interpolate to the “peak” region.

### 3.3 Matching of strange particles to jets and underlying event

The strategy of matching the (multi-)strange particles with jets follow those presented in earlier work [?]. The matching is done on a geometrical basis which presented in Eq. 3.

$$d(\text{particle}, \text{jet}) = \sqrt{(\eta_{\text{particle}} - \eta_{\text{jet}})^2 + (\phi_{\text{particle}} - \phi_{\text{jet}})^2} \quad (3)$$

If the distance between the particle candidate and the jet ( $d$ ) is smaller than the matching distance  $D$  ( $= 0.4$ ), the candidate is considered to be inside the jet cone (JC). The raw yields in JC are not only composed of the hadron produced via jet fragmentation (write as JE), but also hadron from Underlying Event (UE), which is defined as the sum of all particles which are not produced via hard parton fragmentation. The UE contribution is estimated by Perpendicular Cone (PC) yields. The PC indicates the cone, which is located in  $\eta \times \phi$  space in the perpendicular direction to the jet axis at the same  $\eta$ . In addition, the acceptance selections of inclusive (regardless of the association between particle and hard scattering), JC

and UE (multi-)strange particles are different in the  $\eta$ - $\phi$  plane. To get the particle from JE the production yields are normalized to per-acceptance density ( $\rho$ ).

$$\begin{aligned}
 \text{Inclusive : } \quad \frac{d\rho}{dp_T} &= \frac{1}{N_{\text{ev}}} \times \frac{1}{\Delta\eta\Delta\phi} \times \frac{dN}{dp_T} \\
 \text{JC : } \quad \frac{d\rho}{dp_T} &= \frac{1}{N_{\text{ev}}^{\text{jet}}} \times \frac{1}{\mathcal{P}_{\text{JC}}\Delta\eta\Delta\phi} \times \frac{dN}{dp_T} \\
 \text{PC : } \quad \frac{d\rho}{dp_T} &= \frac{1}{N_{\text{ev}}^{\text{jet}}} \times \frac{1}{\mathcal{P}_{\text{PC}}\Delta\eta\Delta\phi} \times \frac{dN}{dp_T}
 \end{aligned} \tag{4}$$

where the  $\mathcal{P}$  denotes the probability of particles in a given selection found in the  $\eta$ - $\phi$  plane with respect to the inclusive one.

### 3.4 Corrections for strange particles reconstruction and feed-down

The reconstruction efficiency of particles are obtained in Monte Carlo simulated data. These are estimated using PYTHIA 8.2 [33] and DPMJet [56] generators in pp and p-Pb, respectively, and transported through a GEANT 3 [57]. Due to different  $\eta$ -shape between particle in JC and the inclusive one, it is needed to take the  $\eta$  dependence of different particle distributions into account [?]. Fig. 2 shows the difference of reconstruction efficiency of JC particles and the inclusive one.

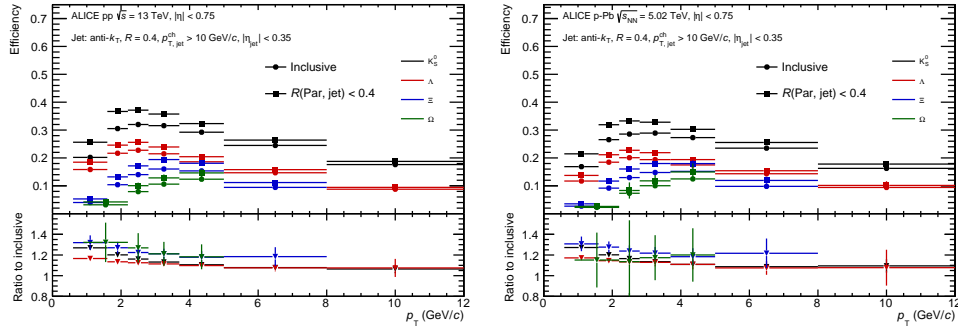


**Figure 2:** The reconstruction efficiency for the particles in pp collisions at  $\sqrt{s} = 13$  TeV (left) and in p-Pb collisions at  $\sqrt{s_{\text{NN}}} = 5.02$  TeV (right) for two selections: inside jet cone,  $R(\text{particle}, \text{jet}) < 0.4$  and the inclusive one.

Only the yields for  $\Lambda$  and  $\bar{\Lambda}$  are significantly affected by secondary particles coming from the decays of charged and neutral  $\Xi$  baryons. The feed-down fraction is calculated with a data-driven approach [24]. The detailed of inclusive feed-down method has been introduced in previous ALICE analysis works [23, 54, 55]. In particular, the  $\Lambda$  and  $\bar{\Lambda}$  in jet and UE feed-down component usually estimated by inclusive  $\Xi^\pm$  spectra and PYTHIA simulations [?], due to lack of  $\Xi^\pm$  in jet and UE results. In this work, the feed-down fraction in jets and UE is computed for each  $p_T$  bin by the measured  $\Xi^\pm$  in jets and UE spectra, thereby assuming that the production rates of charged and neutral  $\Xi$  are equal. Figure 3 shows the results of feed-down fraction in JC and the inclusive one.

### 3.5 Systematic uncertainties

The total systematic uncertainty, for  $K_S^0$ ,  $\Lambda$ ,  $\bar{\Lambda}$ ,  $\Xi^\pm$  and  $\Omega^\pm$  reconstruction of each data point of the final results, due to the choice of selection criteria are estimated separately in each  $p_T$  interval. Individual settings are loosened and tightened, in order to measure changes in the signal loss correction. The main sources of the systematic uncertainty in this measurements are knowledge of detector materials, track selections, particle identification, proper lifetime, topological selection and signal extraction. All these individual error contributions, which are listed in Tab. 3, 4 are added in quadrature.



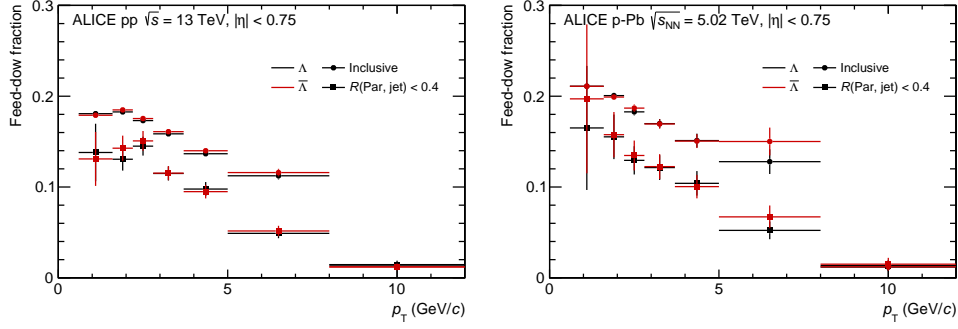


**Figure 3:** Fraction of  $\Lambda$  spectra removed due to feed-down subtraction of charged and neutral  $\Xi$

**Table 3:** Main sources and values of the relative systematic uncertainties(%) of  $K_S^0$ ,  $\Lambda + \bar{\Lambda}$ ,  $\Xi^- + \bar{\Xi}^+$  and  $\Omega^- + \bar{\Omega}^+$  in pp collisions at  $\sqrt{s} = 13$  TeV. The value are reported for low, intermediate and high  $p_T$ .

Uncertainty source	$K_S^0$			$\Lambda + \bar{\Lambda}$			$\Xi^- + \bar{\Xi}^+$			$\Omega^- + \bar{\Omega}^+$			
	$p_T$ (GeV/c)	0.6	2	10	0.6	2	10	0.6	2	7	1	2	5
Detector material		4	4	4	4	4	4	4	4	4	4	4	4
Track selection		1.5	1.2	0.4	0.6	1.4	1.3	2.8	0.1	0.	0.	1.5	0.2
Particle identification		0.1	0.1	0.1	0.3	0.2	1.1	1.9	1.7	2.4	3.9	8.7	6.
Proper lifetime		0	0.1	0	2.1	0.4	0	-	-	-	-	-	-
Topological		0.2	1.4	0	3.9	0.8	3.9	0.6	0.9	1.	2.8	5.4	2.4
Signal extraction		0.8	1.1	1.1	0.3	0.5	1.7	3.	1.	0.5	2.3	4.6	3
Total uncertainty		4.4	4.6	4.2	6.1	4.4	6.1	6.1	4.5	4.8	6.7	12.	8.2

**Table 4:** Main sources and values of the relative systematic uncertainties(%) of  $K_S^0$ ,  $\Lambda + \bar{\Lambda}$ ,  $\Xi^- + \bar{\Xi}^+$  and  $\Omega^- + \bar{\Omega}^+$  in p-Pb collisions at  $\sqrt{s_{NN}} = 5.02$  TeV. The value are reported for low, intermediate and high  $p_T$ .

Uncertainty source	$K_S^0$			$\Lambda + \bar{\Lambda}$			$\Xi^- + \bar{\Xi}^+$			$\Omega^- + \bar{\Omega}^+$			
	$p_T$ (GeV/c)	0.6	2	10	0.6	2	10	0.6	2	7	1	2	5
Detector material		0.4	0.4	0.4	0.4	0.4	0.4	0.4	0.4	0.4	0.4	0.4	0.4
Track selection		1.4	1.7	1.8	0.2	1.3	1.4	0	0	0	1.3	2.5	0
Particle identification		0.1	0.2	0.2	0.3	0.2	1	3.1	1.2	0	8.1	13.7	5.9
Proper lifetime		0	0	0	1.6	0.3	0	0.6	0.4	0	0	3.3	0
Topological		4.4	0.6	1.9	3.9	0.9	2.7	1.3	0	2.6	1.2	4.8	3.7
Signal extraction		0.3	2.6	1.7	0.6	0.5	2.6	5.1	0.9	2.6	0	5.2	0
Total uncertainty		6.1	5.1	5.1	5.8	4.3	5.8	7.4	4.3	5.4	9.2	16.4	8

**Material budget.** The effect of the incomplete knowledge of the detector's material budget is evaluated by comparing different Monte Carlo simulations in which the material budget was increased and decreased by 4.5%. This value corresponds to the uncertainty on the determination of the material budget by measuring photon conversions. This particular systematic uncertainty is around 0.4%.

**Track selection.** To estimate the systematic due to the track selection, the analysis has been redone with the increased number of required clusters in the TPC.



**Particle identification.** The TPC  $dE/dx$  selection is used to reduce the combinatorial background in the (multi-)strange particle invariant mass distribution. The number of  $\sigma$  in the identification of particles using the  $dE/dx$  have been varied between  $4\sigma$  to  $6\sigma$ .

**Proper lifetime selection.** The proper lifetime defined as  $mLc/p$ , which  $m$  is the mass of particles,  $L$  is the decay length, and  $p$  is the particle's momentum. The selection on the  $mLc/p$  is varied from around 12 to 40 cm for  $K_S^0$ , 20 to 40 cm for  $\Lambda$  ( $\bar{\Lambda}$ ) and  $2c\tau$  to  $6c\tau$  for  $\Xi^\pm$  and  $\Omega^\pm$ .

**Topological selection.** The values of the selection criteria on the topological variables are varied around their nominal values. The observed deviations for each component are summed in quadrature.

**Signal extraction.** In the same spirit, the signal extraction technique has been tested by varying the widths used to define the “signal” and “background” regions, expressed in terms of the number of  $\sigma$  as defined in Sec. 3.2.

The additional systematic uncertainty sources associated with particle yield in jet are originated from the UE subtraction estimator and the jet  $p_T$  threshold. The systematic uncertainty due to the UE subtraction is estimated by varying the perpendicular cone radius from the chosen thresholds from 0.4 (PC04) to 0.2 (PC02) and 0.6 (PC06). From the deviation of different PC cone size, the relative systematic uncertainty of the UE subtraction is obtained. To estimate the effect of jet  $p_T$  thresholds uncertainty, the analysis is repeated with the jet  $p_T$  cut  $10 \pm 1$  GeV/ $c$ . The systematic of the particle in jets are added to the list of uncertainties in quadrature. The value are shown in Table 5, 6.

**Table 5:** Main sources and values of the relative systematic uncertainties(%) of  $K_S^0$ ,  $\Lambda + \bar{\Lambda}$ ,  $\Xi^- + \bar{\Xi}^+$  and  $\Omega^- + \bar{\Omega}^+$  in JE in pp collisions at  $\sqrt{s} = 13$  TeV. The value are reported for low, intermediate and high  $p_T$ .

Uncertainty source	$K_S^0$			$\Lambda + \bar{\Lambda}$			$\Xi^- + \bar{\Xi}^+$			$\Omega^- + \bar{\Omega}^+$		
	0.6	2	10	0.6	2	10	0.6	2	7	1	2	5
$p_T$ (GeV/ $c$ )												
Particle reconstruction	1.8	0.25	0.1	5.3	0.6	0	6.7	0.9	0.1	6	1.7	0.3
UE subtraction	0.1	0.1	0.1	0.1	0.2	0.1	1.5	0.2	0.3	3.6	1.8	0.5
Jet $p_T$ threshold	0.6	3.1	10.9	0.6	1.1	9.9	3.5	2.4	5	0	0	0
<b>Total uncertainty</b>	1.8	3.1	10.9	5.3	1.2	9.9	7.7	2.6	5	7.1	2.5	0.6

**Table 6:** Main sources and values of the relative systematic uncertainties(%) of  $K_S^0$ ,  $\Lambda + \bar{\Lambda}$ ,  $\Xi^- + \bar{\Xi}^+$  and  $\Omega^- + \bar{\Omega}^+$  in JE in p-Pb collisions at  $\sqrt{s_{NN}} = 5.02$  TeV. The value are reported for low, intermediate and high  $p_T$ .

Uncertainty source	$K_S^0$			$\Lambda + \bar{\Lambda}$			$\Xi^- + \bar{\Xi}^+$			$\Omega^- + \bar{\Omega}^+$		
	0.6	2	10	0.6	2	10	0.6	2	7	1	2	5
$p_T$ (GeV/ $c$ )												
Particle reconstruction	5	0.8	0	13.2	1.5	0	24.8	2.8	0.3	8.7	3.7	0.9
UE subtraction	0.3	0.1	0.1	0	0.1	11.2	14.1	0.8	0.7	0	0	1.2
Jet $p_T$ threshold	0.3	3.5	11	3.2	1.8	0.1	24.9	3	4.1	3.1	10.7	7.6
<b>Total uncertainty</b>	5	3.6	11	13.5	2.3	11.2	37.9	4.2	4.1	9.3	11.3	7.7

The uncertainty of jet cone particle ratios ( $\Lambda/K_S^0$ ,  $\Xi/K_S^0$ ,  $\Omega/K_S^0$ ,  $\Xi/\Lambda$ ,  $\Omega/\Lambda$  and  $\Omega/\Xi$ ) also consider three sources: the particle reconstruction, UE subtraction and the jet  $p_T$  threshold. The particle reconstruction uncertainty is propagated from the spectra. Uncertainties related to UE subtraction and jet  $p_T$  threshold are obtained by varying the condition in both numerator and denominator of the corresponding ratios.

**Table 7:** Main sources and values of the relative systematic uncertainties(%) of baryon-to-meson ratios ( $\Lambda/K_S^0$ ,  $\Xi/K_S^0$ ,  $\Omega/K_S^0$ ) in JE in pp collisions at  $\sqrt{s} = 13$  TeV. The value are reported for low, intermediate and high  $p_T$ .

Uncertainty source	$(\Lambda + \overline{\Lambda})/(2K_S^0)$			$(\Xi^- + \overline{\Xi}^+)/(2K_S^0)$			$(\Omega^- + \overline{\Omega}^+)/(2K_S^0)$			
	$p_T$ (GeV/c)	0.6	2	10	0.6	2	7	1	2	5
Particle reconstruction		2.4	2.8	2.5	3.4	2.8	2.8	6.7	11.4	7.3
UE subtraction		0.8	0.2	0.4	3.5	0.2	0.1	10	4	2.2
Jet $p_T$ threshold		0.4	2.3	1	1.7	1.6	3.6	1.	3.3	6.4
<b>Total uncertainty</b>		2.6	3.7	2.7	5.2	3.3	4.5	12.4	12.5	10

**Table 8:** Main sources and values of the relative systematic uncertainties(%) of baryon-to-baryon ratios ( $\Xi/\Lambda$ ,  $\Omega/\Lambda$ ,  $\Omega/\Xi$ ) in JE in pp collisions at  $\sqrt{s} = 13$  TeV. The value are reported for low, intermediate and high  $p_T$ .

Uncertainty source	$(\Xi^- + \bar{\Xi}^+)/(\Lambda + \bar{\Lambda})$			$(\Omega^- + \bar{\Omega}^+)/(\Lambda + \bar{\Lambda})$			$(\Omega^- + \bar{\Omega}^+)/(\Xi^- + \bar{\Xi}^+)$			
	$p_T$ (GeV/c)	0.6	2	7	1	2	5	1	2	5
Particle reconstruction		3.4	3	3.2	6.7	11.5	7.5	6.8	11.5	7.4
UE subtraction		4.4	0.4	0.2	12.4	4.2	2.3	7.8	3.8	2.7
Jet $p_T$ threshold		0.7	0.5	1.9	0.2	0.9	3.5	0.4	1.3	3
Total uncertainty		5.6	3	3.7	14.1	12.2	8.6	10.3	12.1	8.5

**Table 9:** Main sources and values of the relative systematic uncertainties(%) of baryon-to-meson ratios ( $\Lambda/K_S^0$ ,  $\Xi/K_S^0$ ,  $\Omega/K_S^0$ ) in JE in p-Pb collisions at  $\sqrt{s_{NN}} = 5.02$  TeV. The value are reported for low, intermediate and high  $p_T$ .

Uncertainty source	$(\Lambda + \bar{\Lambda})/(2K_S^0)$			$(\Xi^- + \bar{\Xi}^+)/(2K_S^0)$			$(\Omega^- + \bar{\Omega}^+)/(2K_S^0)$			
	$p_T$ (GeV/c)	0.6	2	10	0.6	2	7	1	2	5
Particle reconstruction		3.2	3.4	3.3	4.7	3.2	4	9.8	1.5	7.4
UE subtraction		0.8	0.1	0.1	9.1	1.8	1	4.1	0	0.3
Jet $p_T$ threshold		1.4	2.6	0.1	8.6	2.4	6	0.5	1.5	0.3
Total uncertainty		3.6	4.3	3.3	13.4	4.4	7.2	10.6	15.1	7.4

**Table 10:** Main sources and values of the relative systematic uncertainties(%) of baryon-to-baryon ratios ( $\Xi/\Lambda$ ,  $\Omega/\Lambda$ ,  $\Omega/\Xi$ ) in JE in p-Pb collisions at  $\sqrt{s_{NN}} = 5.02$  TeV. The value are reported for low, intermediate and high  $p_T$ .

Uncertainty source	$(\Xi^- + \overline{\Xi}^+)/(\Lambda + \overline{\Lambda})$			$(\Omega^- + \overline{\Omega}^+)/(\Lambda + \overline{\Lambda})$			$(\Omega^- + \overline{\Omega}^+)/(\Xi^- + \overline{\Xi}^+)$			
	$p_T$ (GeV/c)	0.6	2	10	0.6	2	7	1	2	5
Particle reconstruction		4.1	2.8	3.7	9.6	15	7.5	10	14.9	8.6
UE subtraction		9.9	1.9	0.8	3.6	0.1	0.3	11	1.8	0.1
Jet $p_T$ threshold		2.7	0.6	2.6	0.4	5	3	0.4	3.8	1.7
Total uncertainty		11.1	3.4	4.6	10.3	15.8	8.1	14.9	15.5	8.7

## 4 Results and discussion

### 4.1 Particles $p_T$ -differential density

For the strange hadrons discussed in this paper, the ratios of yields for particles and anti-particles are around one within the uncertainties, as expected at these collision energies in the mid-rapidity region. Therefore, all the  $p_T$ -differential density is shown in the following are reported after summing particles and anti-particles. The different selections shown in the following have been introduced in section 3.3, in which also introduced the normalization method.

The  $p_T$ -differential density ( $d\rho/dp_T$  defined by Eq. 4), for all particle species, in pp and MB p-Pb collisions are shown in Fig. 4 and 5, respectively. All the hadrons' densities with  $p_T$  are observed to become harder within events that require at least one charged particle jet with  $p_{T,jet}^{ch} > 10$  GeV/c. Also, as expected, the particle  $p_T$ -differential density in jet is harder than that in underlying events.

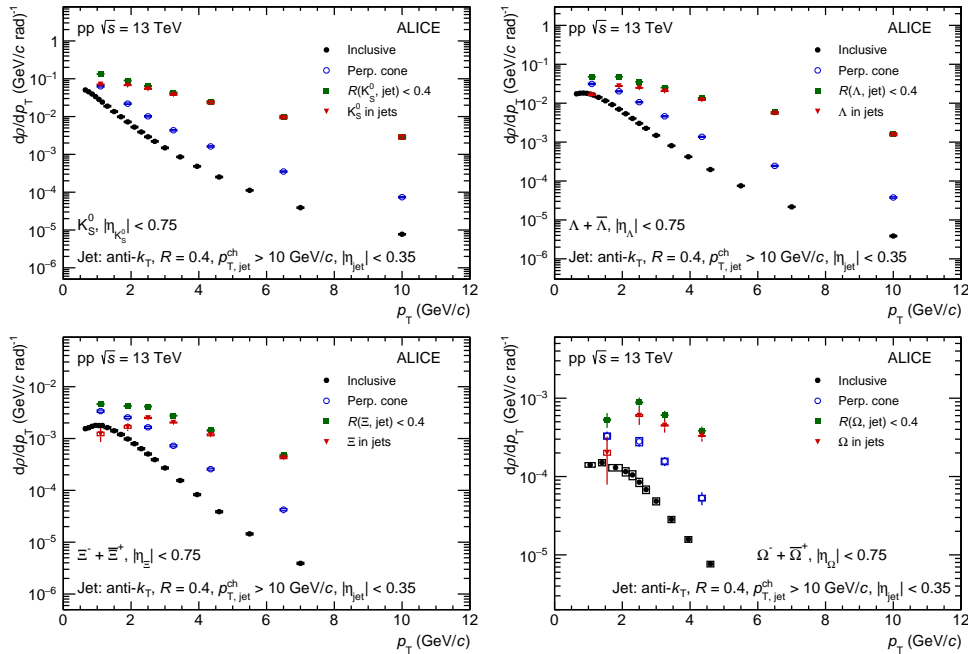


**Figure 4:**  $p_T$ -differential density of  $K_S^0$ ,  $\Lambda + \bar{\Lambda}$ ,  $\Xi^- + \bar{\Xi}^+$  and  $\Omega^- + \bar{\Omega}^+$  in pp at  $\sqrt{s} = 13$  TeV. In those plots, the black point represent particles which from minimum bias events, the green point represent particles which from the jet cones, the blue point represent particles within perpendicular cone of jet which associated with the underlying event and the red point represent the particle from the jet fragmentation.

The  $p_T$  distributions of  $K_S^0$ ,  $\Lambda + \bar{\Lambda}$  and  $\Xi^- + \bar{\Xi}^+$  for the event classes defined in Tab. ?? are shown in Fig. 6. The inclusive distributions become harder with increasing charged-particle multiplicity. Particles in JE, which generated by jet fragmentation, are systematically independent with centrality classes.

### 4.2 Baryon-to-meson and baryon-to-baryon ratios

The  $\Lambda/K_S^0$ ,  $\Xi/K_S^0$  and  $\Omega/K_S^0$  baryon-to-meson ratios and  $\Xi/\Lambda$ ,  $\Omega/\Lambda$  and  $\Omega/\Xi$  baryon-to-baryon ratios are investigated as a function of  $p_T$  for several selections in pp and p-Pb collisions. As can be seen in Figs. 7 (pp at  $\sqrt{s} = 13$  TeV) and 8 (p-Pb at  $\sqrt{s_{NN}} = 5.02$  TeV, 0-100%), the inclusive particle ratios have an enhancement at  $p_T \sim 3 - 4$  GeV/c. Additionally, the same case of particle ratios in underlying events can be observed. However, the particle ratios in jet are significantly lower than the inclusive and UE cases at low and intermediate  $p_T$ . Also the ratios in jet are approximately independent of  $p_T$  beyond 2 GeV/c. This suggests that the ratios of baryon-to-meson and baryon-to-baryon enhancement at intermediate  $p_T$

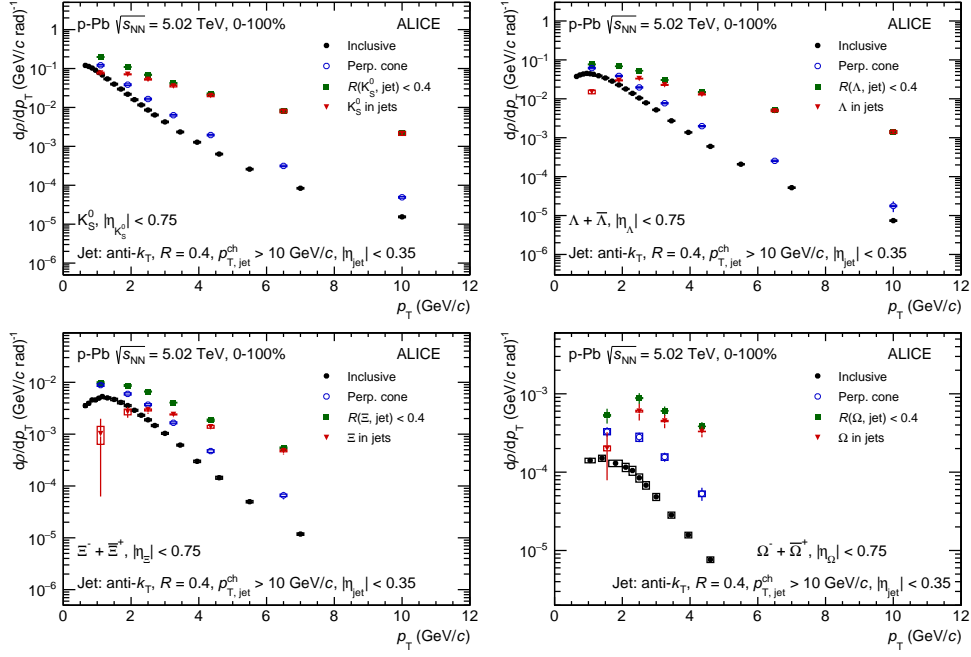


**Figure 5:**  $p_T$ -differential density of  $K_S^0$ ,  $\Lambda + \bar{\Lambda}$ ,  $\Xi^- + \bar{\Xi}^+$  and  $\Omega^- + \bar{\Omega}^+$  in 0-100% in p-Pb at  $\sqrt{s_{NN}} = 5.02$  TeV. In those plots, the black point depicts particles which from minimum bias events, the green point depicts particles which from the jet cones, the blue point depicts particles within perpendicular cone of jet which associated with the underlying event and the red point depicts the particle from the jet fragmentation.

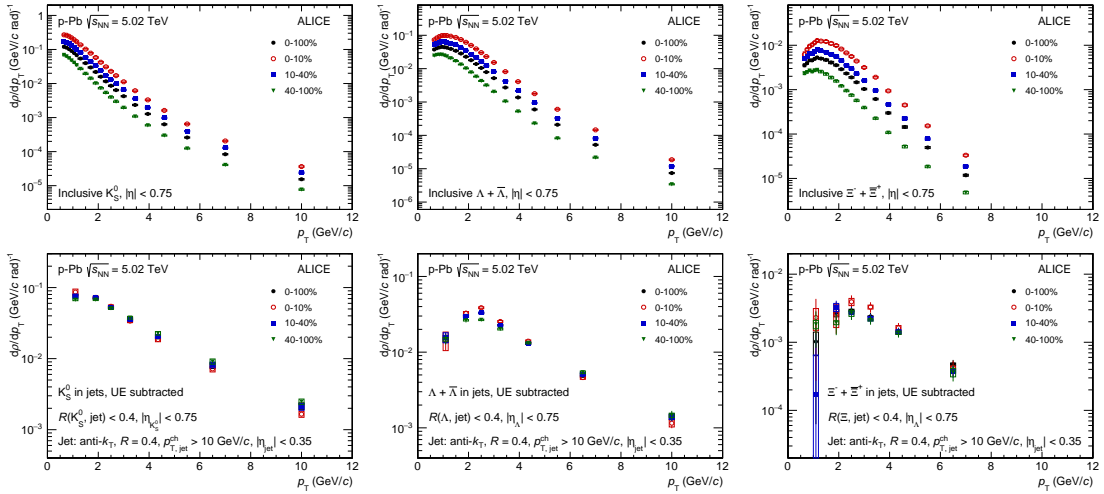


**Figure 6:**  $p_T$ -differential density of  $K_S^0$ ,  $\Lambda + \bar{\Lambda}$  and  $\Xi^- + \bar{\Xi}^+$  in different V0A event centrality classes in p-Pb at  $\sqrt{s_{NN}} = 5.02$  TeV. Top panels show the inclusive particle and bottom panels show particles generated by jet fragmentation. The different centrality classes are depicted with different color.

is not driven by the jet fragmentation.

The particle ratios in jet with centrality and collision system distribution is studied in Fig. 9. The particle ratios in the jet are observed to be relatively centrality and system independent. It is noteworthy that the baryon-to-meson ( $\Lambda/K_S^0$ ,  $\Xi/K_S^0$  and  $\Omega/K_S^0$ ) ratios have a hint of centrality (collision system) dependent for  $2 < p_T < 4$  GeV/c, however this is barely significant given the quoted uncertainties. For  $p_T > 5$  GeV/c, the baryon-to-meson ratios become fairly consistent for all centrality classes and collision systems.

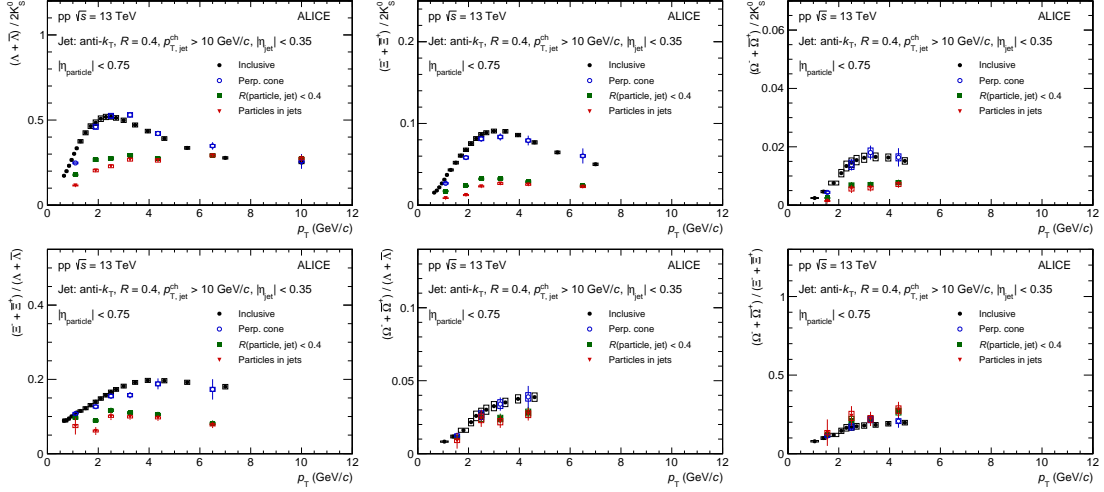


**Figure 7:** The baryon-to-meson (top) and baryon-to-baryon (bottom) ratio as a function of particle  $p_T$  in pp collisions at  $\sqrt{s} = 13$  TeV. In those panels, the black point shows the ratio with particles from minimum bias events, the green point shows the ratio with particles from the jet cones, the blue point shows the ratio with particles from perpendicular cones with jet and the red point shows the ratio with particles that generated by jet.

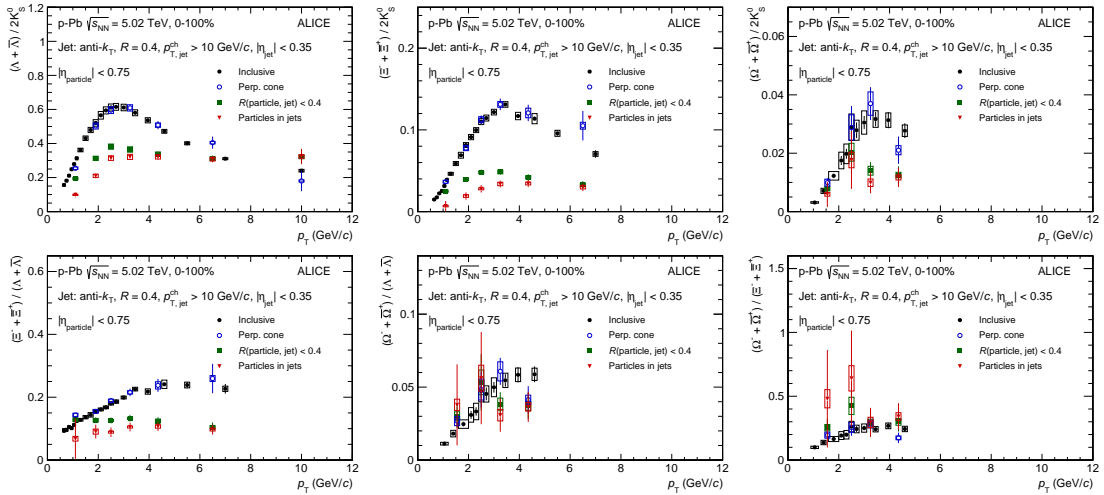


**Figure 8:** The baryon-to-meson (top) and baryon-to-baryon (bottom) ratio as a function of particle  $p_T$  in p-Pb collisions at  $\sqrt{s_{NN}} = 5.02$  TeV. In those panels, the black point shows the ratio with particles from minimum bias events, the green point shows the ratio with particles from the jet cones, the blue point shows the ratio with particles from perpendicular cones with jet and the red point shows the ratio with particles that generated by jet.

### 4.3 Comparison to models

need to be added.

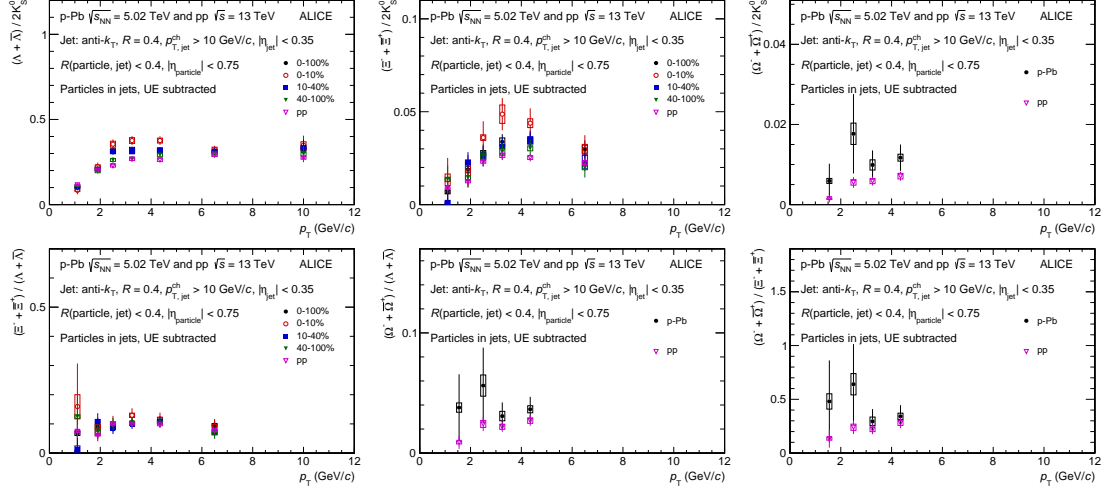


**Figure 9:** The baryon-to-meson (top) and baryon-to-baryon (bottom) ratio as a function of particle  $p_T$  in jets in pp (open symbols) and p-Pb (full symbols). The different centrality classes for p-Pb collisions are depicted with different color.

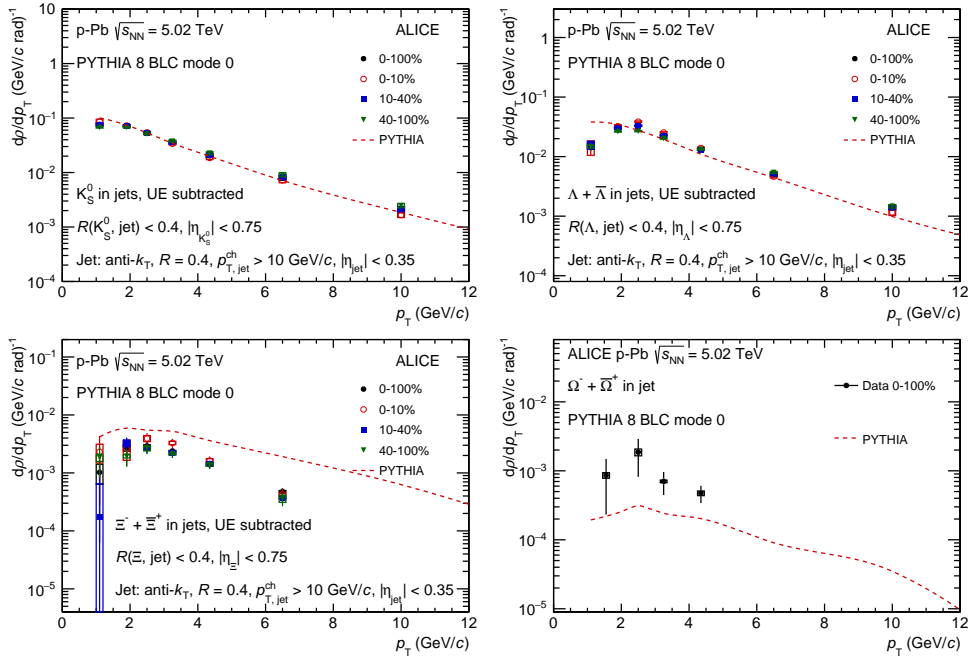


**Figure 10:** Particles in jet in p-Pb at  $\sqrt{s_{NN}} = 5.02$  TeV with PYTHIA 8 BLC mode 0

## 5 Summary

We studied the  $K_S^0$ ,  $\Lambda$  ( $\bar{\Lambda}$ ),  $\Xi^\pm$  and  $\Omega^\pm$   $p_T$ -differential density, the  $\Lambda/K_S^0$ ,  $\Xi/K_S^0$  and  $\Omega/K_S^0$  baryon-to-meson ratio and the  $\Xi/\Lambda$ ,  $\Omega/\Lambda$  and  $\Omega/\Xi$  baryon-to-baryon ratio in jets and underlying events in pp at  $\sqrt{s} = 13$  TeV and p-Pb at  $\sqrt{s_{NN}} = 5.02$  TeV collisions. The main feature of this analysis is the usage of charged particle jet to separate hard and soft progress, providing new insight into the understanding of the origin of flow-like correlations observed in small systems.

The  $p_T$ -differential density in events with charged-particle jet ( $p_{T,jet}^{ch} > 10$  GeV/c) are observed to become harder than that in MB events. Also, the dependence on charged-particle multiplicity found in the inclusive particle is not present for particles generated by jet fragmentation.

The enhancement of baron-to-meson ratio at intermediate  $p_T$  found in the inclusive particle in pp and p-Pb collisions are not present for particles associated with hard scattering. **to be finished**

## Acknowledgements

## References

- [1] J. Rafelski and R. Hagedorn, “From hadron gas to quark matter, 2”,  
<https://cds.cern.ch/record/126179>.
- [2] H. Satz, “Color deconfinement in nuclear collisions”, *Rept. Prog. Phys.* **63** (2000) ,  
[arXiv:hep-ph/0007069](https://arxiv.org/abs/hep-ph/0007069).
- [3] E. V. Shuryak, “Theory and phenomenology of the QCD vacuum”, *Phys. Rept.* **115** (1984) .
- [4] B. V. Jacak and B. Muller, “The exploration of hot nuclear matter”, *Science* **337** (2012) .
- [5] J. Cleymans, R. Gavai, and E. Suhonen, “Quarks and Gluons at High Temperatures and Densities”, *Phys. Rept.* **130** (1986) .
- [6] S. Bass, M. Gyulassy, H. Stoecker, and W. Greiner, “Signatures of quark gluon plasma formation in high-energy heavy ion collisions: A Critical review”, *J. Phys. G* **25** (1999) ,  
[arXiv:hep-ph/9810281](https://arxiv.org/abs/hep-ph/9810281).
- [7] P. Braun-Munzinger and J. Stachel, “The quest for the quark-gluon plasma”, *Nature* **448** (2007) .
- [8] E. Laermann and O. Philipsen, “The Status of lattice QCD at finite temperature”, *Ann. Rev. Nucl. Part. Sci.* **53** (2003) , [arXiv:hep-ph/0303042](https://arxiv.org/abs/hep-ph/0303042).
- [9] S. Gupta, X. Luo, B. Mohanty, H. G. Ritter, and N. Xu, “Scale for the Phase Diagram of Quantum Chromodynamics”, *Science* **332** (2011) , [arXiv:1105.3934](https://arxiv.org/abs/1105.3934) [hep-ph].
- [10] T. Bhattacharya *et al.*, “QCD Phase Transition with Chiral Quarks and Physical Quark Masses”, *Phys. Rev. Lett.* **113** no. 8, (2014) , [arXiv:1402.5175](https://arxiv.org/abs/1402.5175) [hep-lat].
- [11] C. Salgado *et al.*, “Proton-Nucleus Collisions at the LHC: Scientific Opportunities and Requirements”, *J. Phys. G* **39** (2012) , [arXiv:1105.3919](https://arxiv.org/abs/1105.3919) [hep-ph].
- [12] K. J. Eskola, P. Paakkinen, H. Paukkunen, and C. A. Salgado, “EPPS16: Nuclear parton distributions with LHC data”, *Eur. Phys. J. C* **77** no. 3, (2017) , [arXiv:1612.05741](https://arxiv.org/abs/1612.05741) [hep-ph].
- [13] ALICE Collaboration, S. Acharya *et al.*, “Investigations of Anisotropic Flow Using Multiparticle Azimuthal Correlations in pp, p-Pb, Xe-Xe, and Pb-Pb Collisions at the LHC”, *Phys. Rev. Lett.* **123** no. 14, (2019) , [arXiv:1903.01790](https://arxiv.org/abs/1903.01790) [nucl-ex].



- [14] **ATLAS** Collaboration, G. Aad *et al.*, “Observation of Long-Range Elliptical Anisotropies in  $\sqrt{s}=13$  and 2.76 TeV  $pp$  Collisions with the ATLAS Detector”, *Phys. Rev. Lett.* **116** no. 17, (2016), [arXiv:1509.04776 \[hep-ex\]](#).
- [15] **ALICE** Collaboration, B. Abelev *et al.*, “Long-range angular correlations on the near and away side in  $p$ -Pb collisions at  $\sqrt{s_{NN}}=5.02$  TeV”, *Phys. Lett. B* **719** (2013), [arXiv:1212.2001 \[nucl-ex\]](#).
- [16] **ALICE** Collaboration, B. B. Abelev *et al.*, “Long-range angular correlations of  $\pi$ , K and p in p-Pb collisions at  $\sqrt{s_{NN}}=5.02$  TeV”, *Phys. Lett. B* **726** (2013), [arXiv:1307.3237 \[nucl-ex\]](#).
- [17] **CMS** Collaboration, V. Khachatryan *et al.*, “Evidence for Collective Multiparticle Correlations in p-Pb Collisions”, *Phys. Rev. Lett.* **115** no. 1, (2015), [arXiv:1502.05382 \[nucl-ex\]](#).
- [18] **ALICE** Collaboration, B. B. Abelev *et al.*, “ $K^*(892)^0$  and  $\phi(1020)$  production in Pb-Pb collisions at  $\sqrt{s_{NN}}=2.76$  TeV”, *Phys. Rev. C* **91** (2015), [arXiv:1404.0495 \[nucl-ex\]](#).
- [19] **ALICE** Collaboration, J. Adam *et al.*, “Multi-strange baryon production in p-Pb collisions at  $\sqrt{s_{NN}}=5.02$  TeV”, *Phys. Lett. B* **758** (2016), [arXiv:1512.07227 \[nucl-ex\]](#).
- [20] **ALICE** Collaboration, S. Acharya *et al.*, “Multiplicity dependence of light-flavor hadron production in pp collisions at  $\sqrt{s}=7$  TeV”, *Phys. Rev. C* **99** no. 2, (2019), [arXiv:1807.11321 \[nucl-ex\]](#).
- [21] **CMS** Collaboration, V. Khachatryan *et al.*, “Multiplicity and rapidity dependence of strange hadron production in pp, pPb, and PbPb collisions at the LHC”, *Phys. Lett. B* **768** (2017), [arXiv:1605.06699 \[nucl-ex\]](#).
- [22] **ALICE** Collaboration, B. B. Abelev *et al.*, “ $K_S^0$  and  $\Lambda$  production in Pb-Pb collisions at  $\sqrt{s_{NN}}=2.76$  TeV”, *Phys. Rev. Lett.* **111** (2013), [arXiv:1307.5530 \[nucl-ex\]](#).
- [23] **ALICE** Collaboration, J. Adam *et al.*, “Enhanced production of multi-strange hadrons in high-multiplicity proton-proton collisions”, *Nature Phys.* **13** (2017), [arXiv:1606.07424 \[nucl-ex\]](#).
- [24] **ALICE** Collaboration, B. B. Abelev *et al.*, “Multiplicity Dependence of Pion, Kaon, Proton and Lambda Production in p-Pb Collisions at  $\sqrt{s_{NN}}=5.02$  TeV”, *Phys. Lett. B* **728** (2014), [arXiv:1307.6796 \[nucl-ex\]](#).
- [25] **ALICE** Collaboration, S. Acharya *et al.*, “Measurements of inclusive jet spectra in pp and central Pb-Pb collisions at  $\sqrt{s_{NN}}=5.02$  TeV”, *Phys. Rev. C* **101** no. 3, (2020), [arXiv:1909.09718 \[nucl-ex\]](#).
- [26] **ALICE** Collaboration, S. Acharya *et al.*, “Measurement of charged jet cross section in  $pp$  collisions at  $\sqrt{s}=5.02$  TeV”, *Phys. Rev. D* **100** no. 9, (2019), [arXiv:1905.02536 \[nucl-ex\]](#).
- [27] **ALICE** Collaboration, B. B. Abelev *et al.*, “Charged jet cross sections and properties in proton-proton collisions at  $\sqrt{s}=7$  TeV”, *Phys. Rev. D* **91** no. 11, (2015), [arXiv:1411.4969 \[nucl-ex\]](#).
- [28] **ALICE** Collaboration, B. Abelev *et al.*, “Measurement of the inclusive differential jet cross section in  $pp$  collisions at  $\sqrt{s}=2.76$  TeV”, *Phys. Lett. B* **722** (2013), [arXiv:1301.3475 \[nucl-ex\]](#).

- [29] ALICE Collaboration, S. Acharya *et al.*, “Charged jet cross section and fragmentation in proton-proton collisions at  $\sqrt{s} = 7$  TeV”, *Phys. Rev. D* **99** no. 1, (2019) , [arXiv:1809.03232 \[nucl-ex\]](#).
- [30] ALICE Collaboration, S. Acharya *et al.*, “Constraints on jet quenching in p-Pb collisions at  $\sqrt{s_{NN}} = 5.02$  TeV measured by the event-activity dependence of semi-inclusive hadron-jet distributions”, *Phys. Lett. B* **783** (2018) , [arXiv:1712.05603 \[nucl-ex\]](#).
- [31] ALICE Collaboration, J. Adam *et al.*, “Measurement of dijet  $k_T$  in p-Pb collisions at  $\sqrt{s_{NN}}=5.02$  TeV”, *Phys. Lett. B* **746** (2015) , [arXiv:1503.03050 \[nucl-ex\]](#).
- [32] ALICE Collaboration, J. Adam *et al.*, “Centrality dependence of charged jet production in p-Pb collisions at  $\sqrt{s_{NN}} = 5.02$  TeV”, *Eur. Phys. J. C* **76** no. 5, (2016) , [arXiv:1603.03402 \[nucl-ex\]](#).
- [33] T. Sjöstrand, S. Ask, J. R. Christiansen, R. Corke, N. Desai, P. Ilten, S. Mrenna, S. Prestel, C. O. Rasmussen, and P. Z. Skands, “An introduction to PYTHIA 8.2”, *Comput. Phys. Commun.* **191** (2015) , [arXiv:1410.3012 \[hep-ph\]](#).
- [34] ALICE Collaboration, K. Aamodt *et al.*, “The ALICE experiment at the CERN LHC”, *Journal of Instrumentation* **3** no. 08, (Aug, 2008) .
- [35] ALICE Collaboration, B. B. Abelev *et al.*, “Performance of the ALICE Experiment at the CERN LHC”, *Int. J. Mod. Phys. A* **29** (2014) , [arXiv:1402.4476 \[nucl-ex\]](#).
- [36] ALICE Collaboration, E. Abbas *et al.*, “Performance of the ALICE VZERO system”, *JINST* **8** (2013) , [arXiv:1306.3130 \[nucl-ex\]](#).
- [37] ALICE Collaboration, K. Aamodt *et al.*, “Alignment of the ALICE Inner Tracking System with cosmic-ray tracks”, *JINST* **5** (2010) , [arXiv:1001.0502 \[physics.ins-det\]](#).
- [38] J. Alme *et al.*, “The ALICE TPC, a large 3-dimensional tracking device with fast readout for ultra-high multiplicity events”, *Nucl. Instrum. Meth. A* **622** (2010) , [arXiv:1001.1950 \[physics.ins-det\]](#).
- [39] ALICE TOF Collaboration, A. Akindinov *et al.*, “Particle identification with the ALICE TOF detector at very high particle multiplicity”, *Eur. Phys. J. C* **32S1** (2004) .
- [40] A. Akindinov *et al.*, “The ALICE Time-Of-Flight system: Construction, assembly and quality tests”, *Nuovo Cim. B* **124** (2009) .
- [41] A. Akindinov *et al.*, “Results of the ALICE time-of-flight detector from the 2009 cosmic-ray data taking”, *Eur. Phys. J. C* **68** (2010) .
- [42] ALICE Collaboration, F. Carnesecchi, “Performance of the ALICE Time-Of-Flight detector at the LHC”, *JINST* **14** no. 06, (2019) , [arXiv:1806.03825 \[physics.ins-det\]](#).
- [43] ALICE Collaboration, “ALICE luminosity determination for pp collisions at  $\sqrt{s} = 13$  TeV”, <http://cds.cern.ch/record/2160174>.
- [44] ALICE Collaboration, “Measurement of visible cross sections in proton-lead collisions at  $\sqrt{s_{NN}} = 5.02$  tev in van der meer scans with the alice detector”, *Journal of Instrumentation* **9** no. 11, (Nov, 2014) . <http://dx.doi.org/10.1088/1748-0221/9/11/P11003>.
- [45] ALICE Collaboration, J. Adam *et al.*, “Pseudorapidity and transverse-momentum distributions of charged particles in proton-proton collisions at  $\sqrt{s} = 13$  TeV”, *Phys. Lett. B* **753** (2016) , [arXiv:1509.08734 \[nucl-ex\]](#).

- [46] M. Cacciari, G. P. Salam, and G. Soyez, “FastJet User Manual”, *Eur. Phys. J. C* **72** (2012), [arXiv:1111.6097 \[hep-ph\]](#).
- [47] M. Cacciari, G. P. Salam, and G. Soyez, “The anti- $k_t$  jet clustering algorithm”, *JHEP* **04** (2008), [arXiv:0802.1189 \[hep-ph\]](#).
- [48] M. Cacciari and G. P. Salam, “Pileup subtraction using jet areas”, *Phys. Lett. B* **659** (2008), [arXiv:0707.1378 \[hep-ph\]](#).
- [49] M. Cacciari, G. P. Salam, and G. Soyez, “The Catchment Area of Jets”, *JHEP* **04** (2008), [arXiv:0802.1188 \[hep-ph\]](#).
- [50] CMS Collaboration, S. Chatrchyan *et al.*, “Measurement of the underlying event activity in  $pp$  collisions at  $\sqrt{s} = 0.9$  and 7 TeV with the novel jet-area/median approach”, *JHEP* **08** (2012), [arXiv:1207.2392 \[hep-ex\]](#).
- [51] Particle Data Group Collaboration, M. Tanabashi *et al.*, “Review of Particle Physics”, *Phys. Rev. D* **98** (Aug, 2018).
- [52] ALICE Collaboration, K. Aamodt *et al.*, “Strange particle production in proton-proton collisions at  $\sqrt{s} = 0.9$  TeV with ALICE at the LHC”, *Eur. Phys. J. C* **71** (2011), [arXiv:1012.3257 \[hep-ex\]](#).
- [53] ALICE Collaboration, B. Abelev *et al.*, “Multi-strange baryon production in  $pp$  collisions at  $\sqrt{s} = 7$  TeV with ALICE”, *Phys. Lett. B* **712** (2012), [arXiv:1204.0282 \[nucl-ex\]](#).
- [54] ALICE Collaboration, S. Acharya *et al.*, “Production of light-flavor hadrons in  $pp$  collisions at  $\sqrt{s} = 7$  and  $\sqrt{s} = 13$  TeV”, [arXiv:2005.11120 \[nucl-ex\]](#).
- [55] ALICE Collaboration, S. Acharya *et al.*, “Multiplicity dependence of (multi-)strange hadron production in proton-proton collisions at  $\sqrt{s} = 13$  TeV”, *Eur. Phys. J. C* **80** no. 2, (2020), [arXiv:1908.01861 \[nucl-ex\]](#).
- [56] S. Roesler, R. Engel, and J. Ranft, “The Monte Carlo event generator DPMJET-III”, in *International Conference on Advanced Monte Carlo for Radiation Physics, Particle Transport Simulation and Applications (MC 2000)*, pp. 1033–1038. 12, 2000. [arXiv:hep-ph/0012252](#).
- [57] R. Brun, F. Bruyant, F. Carminati, S. Giani, M. Maire, A. McPherson, G. Patrick, and L. Urban, “GEANT Detector Description and Simulation Tool”,.

388 **A The ALICE Collaboration**